

# Unusually large magnetic moments in the normal state and superconducting state of Sn nanoparticles

Chi-Hang Hung · Chi-Hung Lee ·  
Chien-Kang Hsu · Chi-Yen Li · Sunil K. Karna ·  
Chin-Wei Wang · Chun-Ming Wu · Wen-Hsien Li

Received: 5 May 2013 / Accepted: 26 July 2013 / Published online: 9 August 2013  
© Springer Science+Business Media Dordrecht 2013

**Abstract** We report on the observations of spontaneous magnetic moments in the normal as well as in the superconducting states of a 9 nm Sn nanoparticle assembly, through X-ray diffraction, magnetization, ac magnetic susceptibility, and neutron diffraction measurements. The saturation magnetization reaches an unexpectedly large value of 1.04 emu/g at 5 K, with a temperature profile that can be described by Bloch's law with an exponent of  $b = 1.8$ . A magnetic moment of  $\langle \mu_Z \rangle = 0.38 \mu_B$  develops after cooling from 260 to 4 K. Superconductivity develops below  $T_C = 3.98$  K, which is 7 % higher than the  $T_C = 3.72$  K of bulk Sn. Surprisingly, an additional magnetic moment of  $\langle \mu_Z \rangle = 0.05 \mu_B$  develops upon entering the superconducting state.

**Keywords** Sn nanoparticle · Superconductivity · Ferromagnetism

## Introduction

In its bulk form, the group IV element Sn crystallizes into a tetragonal  $I4_1/amd$  symmetry, known as  $\beta$ -Sn, at

room temperature, but transform into a cubic Fd3m symmetry, known as  $\alpha$ -Sn, below 286.4 K. It displays a diamagnetic response to an applied magnetic field, and superconductivity develops below  $T_C = 3.72$  K with a relatively weak critical magnetic field of  $H_C = 305$  Oe at zero temperature. The appearance of superconductivity in bulk Sn is known to originate from the formations of spin single  $s$ -wave Cooper pairs. Although Cooper-pair moment has been observed in  $Sr_2RuO_4$  in polarized neutron diffraction studies (Duffy et al. 2000), the appearance of a ferromagnetic moment in the superconducting state is not anticipated to occur in the spin-singlet paired bulk Sn. However, the electron and lattice characteristics can be greatly modified, when the size of the systems is reduced to the nanometer scale (Bezryadin et al. 2000; Reich et al. 2003; Li et al. 2003, 2005, 2008, 2011; Bose et al. 2005, 2010; Guo et al. 2004; LeClair et al. 2005). Noticeable enhancements of  $T_C$  and  $H_C$  have been observed in extremely space-restricted Pb (Li et al. 2003), In (Li et al. 2005), Sn (Li et al. 2008), and Al (Liu et al. 2011) nanoparticles before reaching the Anderson regime. In addition, spin polarized moments have also been found in many elements, such as Au, Ag, In, Sn, Pd, and Pb (Yamamoto et al. 2004; Hori et al. 2004; Wu et al. 2010; Crespo et al. 2004; Karna et al. 2011), in their nanoparticle forms. However, the magnetic moments associated with these polarized spins are relatively weak, amounting to only about 1–5 % of the atoms in the particles being magnetic with a saturation magnetization in the order

C.-H. Hung · C.-H. Lee · C.-K. Hsu ·  
C.-Y. Li · S. K. Karna · C.-W. Wang ·  
C.-M. Wu · W.-H. Li (✉)

Department of Physics and Center for Neutron Beam  
Applications, National Central University,  
Jhongli 32001, Taiwan  
e-mail: whli@phy.ncu.edu.tw

of  $10^{-2}$  emu/g (Yamamoto et al. 2004; Hori et al. 2004; Wu et al. 2010). In this article, we report on the results of studies made on the magnetic behavior of Sn nanoparticle assembly in the normal state and superconducting state. An unexpectedly large saturation magnetization of 1.04 emu/g is observed at 5 K, which decreases by only 8 %, when the temperature is increased to 300 K. Intrinsic magnetic moments persist in the superconducting state below  $T_C = 3.98$  K, where Meissner screenings are clearly revealed. Surprisingly, the thermal reduction rate of the magnetic moment in the superconducting state is a factor of 15 higher than that in the normal state, showing that there is a magnetic component directly associated with the superconducting state.

## Materials

The Sn nanoparticles are fabricated by employing the gas-condensation method. High-purity (99.99 %) Sn spheres ( $\sim 2.5$  mm in diameter) are evaporated in an Ar atmosphere with a pressure of 1 torr, using an evaporation rate of  $0.05 \text{ \AA/s}$ . The evaporated particles are collected on a non-magnetic plate, which is placed 20 cm above the evaporation source and maintained at 77 K. After restoration to room temperature, the nanoparticles, which are only loosely attached to the collector, are stripped off the collector plate. The sample thus obtained is in a powdered form and consists of a macroscopic amount of individual Sn nanoparticles. There is no substrate or capping molecule on these nanoparticles. The nanoparticles are kept in a vacuum at all times.

X-ray diffraction (XRD), atomic force microscopy (AFM), transmission electron microscopy (TEM), X-ray fluorescence spectroscopy (XRFS), energy dispersive X-ray spectroscopy (EDXS), and atomic absorption spectroscopy (AAS) are used to characterize the sample. Size analysis based on the AFM and TEM images reveal that the size distribution of the nanoparticle assembly can be described using a lognormal distribution, as shown in the inset to Fig. 1 (vertical bars). The X-ray and neutron diffraction patterns show that the nanoparticles crystallize into the same  $\beta$ -Sn structure as their bulk counterpart at 300 K, and remain a  $\beta$ -Sn structure upon cooling to 1.65 K (the lowest temperature achieved in this study). The diffraction peaks appear to be much

broader than the instrumental resolution, reflecting the finite-size effect. The mean particle diameter is determined by fitting the diffraction peaks to the diffraction profiles of finite sized particles, assuming a lognormal size distribution for the nanoparticle assembly. Figure 1 shows the observed (crosses) and fitted (solid curves) XRD patterns obtained at 300 K, where the solid curves indicate the calculated pattern assuming a lognormal size distribution (dashed curve in the inset to Fig. 1) with a center at 9 nm and a half-width of 1.3 nm. This size distribution obtained from the XRD peak profiles agrees well with that obtained from the AFM and TEM images (vertical bars) shown in the inset to Fig. 1.

Chemical analysis by means of XRFS and AAS has also been performed to search for impurities. The XRFS spectra are taken on a Rigaku ZSK Primus II spectrometer, employing the standard setup to scan through 15 mg of the Sn nanoparticles. No fluorescence lines other than those from Sn are detected. The AAS spectra are taken on a Perkin-Elmer Analyst 700 spectrometer, employing a graphite furnace and a cathode discharge lamp aims for detecting Fe and Ni. No traces of such elements are found within the resolution limitation of 50 parts per million. Note that a molar ratio of  $O/Sn = 1/10$  would be expected if a 9 nm Sn particle is to be covered by a single O layer. This amount of oxygen atoms is easily detectable by

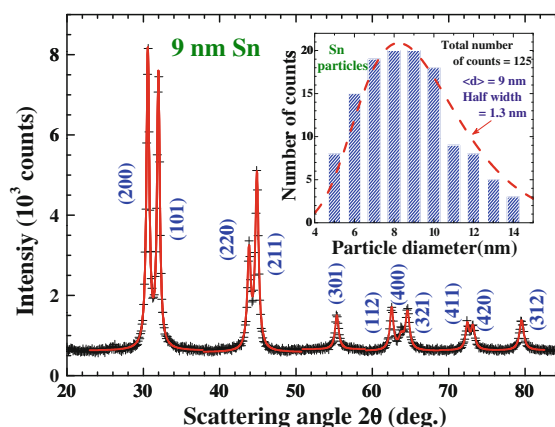


**Fig. 1** X-ray diffraction pattern of the 9 nm Sn particle assembly at 300 K, revealing a tetragonal  $\beta$ -Sn structure. Line broadening, resulting from the finite-size effect, can be clearly seen in the diffraction profiles. The *solid curves* indicate the calculated pattern assuming a lognormal size distribution with a center at 9 nm and a half-width of 1.3 nm. The *inset* shows the size distributions obtained from X-ray diffraction profile (*dashed curve*) and from AFM and TEM images (*vertical bars*)

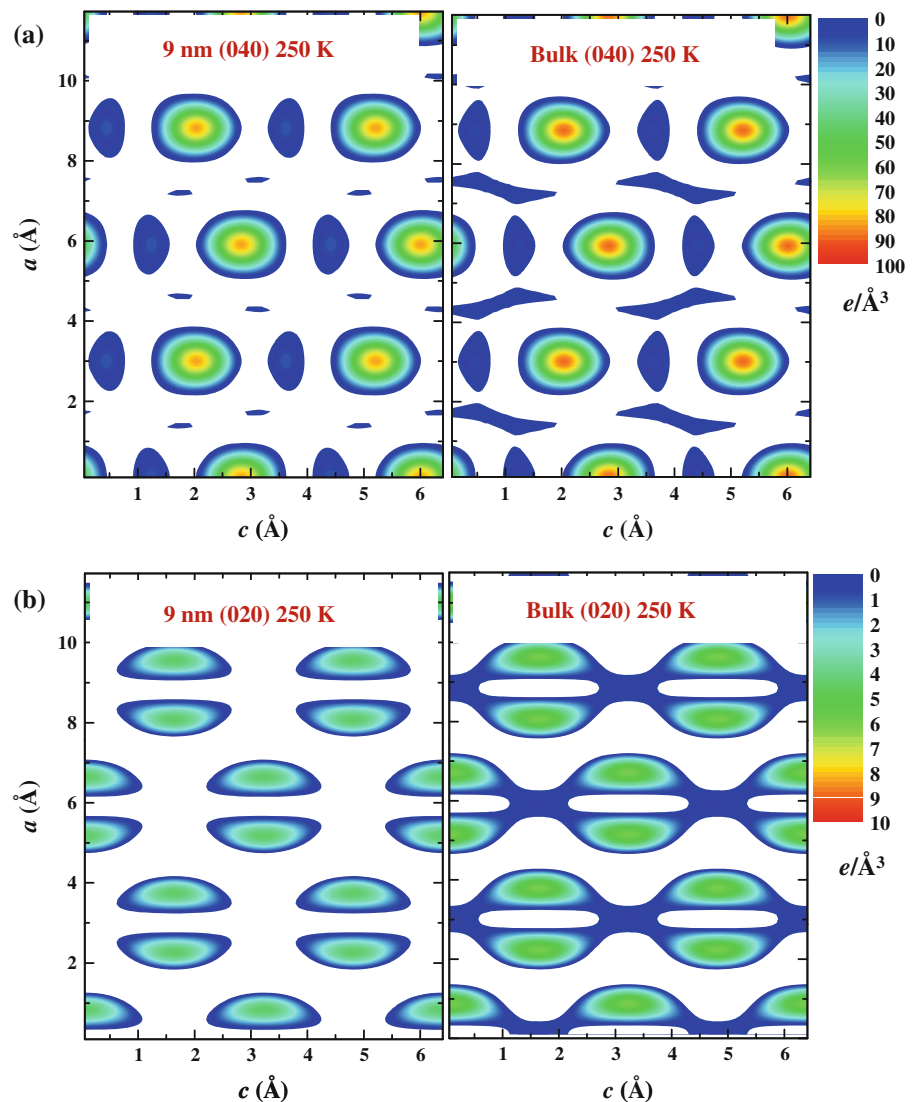
both XRFs and AAS analyses. There are no identifiable traces of oxidation phases or elements other than Sn in the XRD/EDXS/XRFs/AAS spectra.

## Results and discussion

Interestingly, the electronic charge distribution of the 9 nm particles is found to be very different from that of bulk Sn. Figure 2a, b displays the electronic charge density contour maps in the (040) and (020) planes, respectively, of the 9 nm and bulk Sn at 250 K, as inferred from the XRD data. These electron density maps were obtained employing the General Structure

Analysis System (GSAS) program (Larson and von Dreele 1990), starting with profile refining the XRD pattern, followed by calculating the inverse Fourier transforms of the structure factors to extract the electron density distribution. The electron density contour map of a specific plane was then obtained by slicing the electron density in the vicinity, covering 0.025 Å below and above the plane. It is clear that the electronic charges of the 9 nm particles are more localized around the lattice site and the inter-tetragonal layers ( $a$ - $c$  planes) are less bounded to each other. The effects of quantum confinement are not yet significant, as the average Kubo level separation  $\Delta = 0.19$  meV (Halperin 1986). It is then mainly the

**Fig. 2** Electronic charge density maps in the **a** (040) and **b** (020) lattice planes of 9 nm and bulk Sn at 250 K, as inferred from X-ray diffraction data. Note that the intensity *scale bar* in **(b)** is a factor of 10 smaller than that of **(a)**



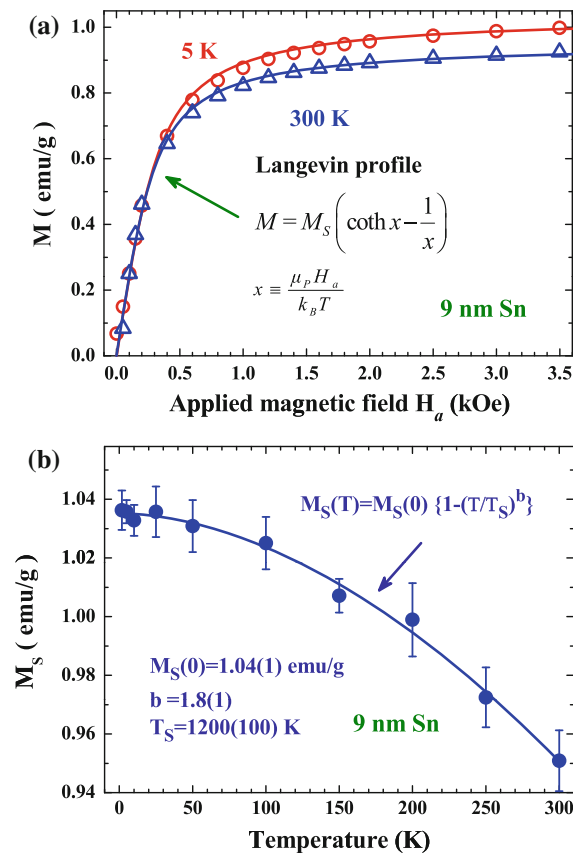


**Fig. 3** **a** Representative  $M(H_a)$  curves of the 9 nm Sn particle assembly at 5 and 300 K. The solid curves indicate the results of fits to Langevin profile. **b** Temperature dependence of the saturation magnetization. The solid curve indicates the results of fits to Bloch's law listed in the plot, giving a critical exponent of  $b = 1.8$

small size effect that originates from the disruption of lattice periodicity at the particle surface drives the charge redistribution.

Magnetization and ac magnetic susceptibility measurements are performed on a Physical Property Measurement System manufactured by Quantum Design, employing the standard setup. For the magnetization and susceptibility measurements, the nanoparticles ( $\sim 40$  mg) are packed into a non-magnetic cylindrical holder, which produces a smooth temperature curve and background signals that are  $\sim 2\%$  that of the sample. The packing fraction  $f$  of the nanoparticle assembly is typically 5%, which indicates the ratio of the mass densities of the assembly to that of its bulk counterpart.

Figure 3a displays the variations in the magnetization  $M$  with the applied magnetic field  $H_a$ , taken at

representative 5 and 300 K. The magnetization increases rapidly with increasing  $H_a$ , becoming saturated at  $H_a \sim 1.5$  kOe. This signifies the existence of a spin polarized moment in the 9 nm Sn particle assembly. The  $M(H_a)$  curve may be satisfactorily described by a Langevin profile (solid curve) to extract saturation magnetization  $M_S$  and mean particle moment  $\mu_p$ . The Langevin  $M(H_a)$  profile may be understood as a randomly oriented assembly of non-interacting magnetic Sn nanoparticles that are being aligned by  $H_a$ . Magnetic hysteresis appears in the low  $H_a$  regime before  $M$  reaches saturation at all temperatures studied, revealing a positive remanence of  $M_R = 0.08$  emu/g at 300 K. Figure 3b displays the  $M_S(T)$  curve that is obtained in the field-increasing processes.  $M_S$  reaches 1.04 emu/g at 5 K, which is 2% of the magnetic moment of bulk Ni. There was no expectation that Sn nanoparticles would develop such a large magnetic moment. The  $M_S(T)$  curve can be described (solid curve) by a power law, as listed in the plot, but with an exponent of  $b = 1.8$ . This value of  $b = 1.8$  lies between the  $b = 3/2$  (known as Bloch's law) expected for creations of thermal magnons in bulk systems (Kittel 1996) and the  $b = 2$  expected on a mean field calculation for finite-size ferromagnetic clusters (Hendriksen et al. 1992).

The saturation magnetization is found to be varied significantly with particle size. The  $M(H_a)$  curves of three representative particle sizes, taken at 300 K, are shown in Fig. 4a. These  $M(H_a)$  curves may be satisfactorily described by Langevin profiles (solid curves) as well. Saturation magnetization of the 11 nm particles reaches 1.52 emu/g at 300 K, while that of the 3.3 nm particles drops to 0.01 emu/g. Figure 4b displays the size dependence of  $M_S$  at 300 K. Large saturation magnetizations are seen for particles with diameters between 7 and 13 nm. It is interesting to note that  $M_S$  decreases with decreasing particle size for particles smaller than 11 nm, showing that the development of magnetic moments in Sn nanoparticles cannot be solely associated with the surface effect. We remark further that saturation magnetizations of all the Sn nanoparticles studied hardly decrease (all less than 20%) from 5 to 300 K, resulting in remarkably high transition temperatures for the Sn nanoparticles when are expressed using the Bloch's expression. There is, however, no experimental evidence to support that  $M_S(T)$  of Sn nanoparticles would indeed follow the same power law at higher temperatures. It is difficult to

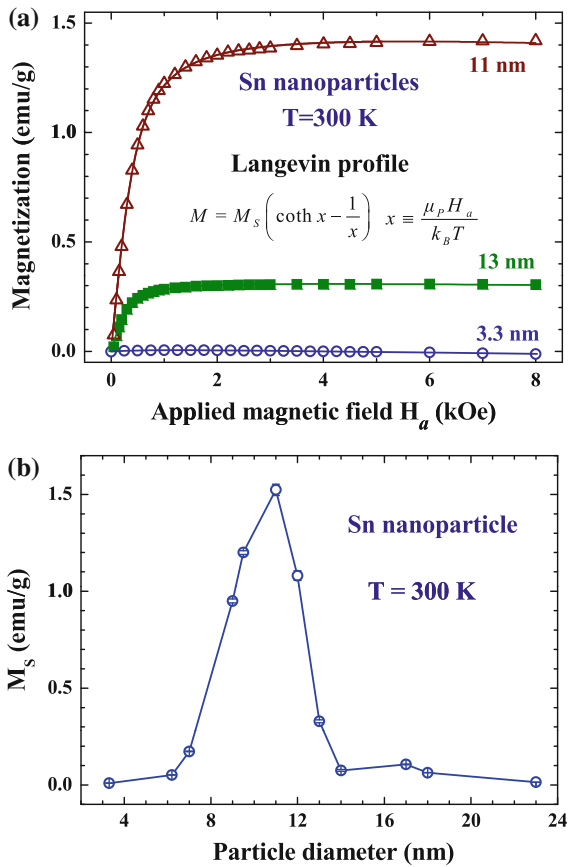


**Fig. 4** **a**  $M(H_a)$  curves of various Sn particle assemblies, taken at 300 K. The *solid curves* indicate the results of fits to Langevin profile. **b** Variations of the saturation magnetization at 300 K with particle diameter, revealing the appearance of unusual large magnetic moments for particles with diameters between 7 and 13 nm

perform measurements at above 300 K without initiating the influences from annealing.

Figure 5a shows the temperature dependence of the in-phase  $\chi'$  and the out-of-phase  $\chi''$  components of the ac magnetic susceptibility. Diamagnetic responses in  $\chi'$  together with sharp increases of  $\chi''$  that signal the occurrence of superconductivity are revealed below  $\sim 4$  K. The  $\chi'(T)$  can be described (solid curves) by Scalapino's expression (Mühschlegel et al. 1972) to give  $T_C = 3.98(2)$  K, which is 7 % higher than the  $T_C = 3.72$  K of bulk Sn. The effects of  $H_a$  on the superconducting screening depart dramatically from the constant behavior expected for bulk Sn, as shown in Fig. 5b. The maximum screening appears at  $H_{C1} = 605(8)$  Oe, which is a factor of 2 higher than  $H_C = 305$  Oe of bulk Sn. Beyond which the weakening

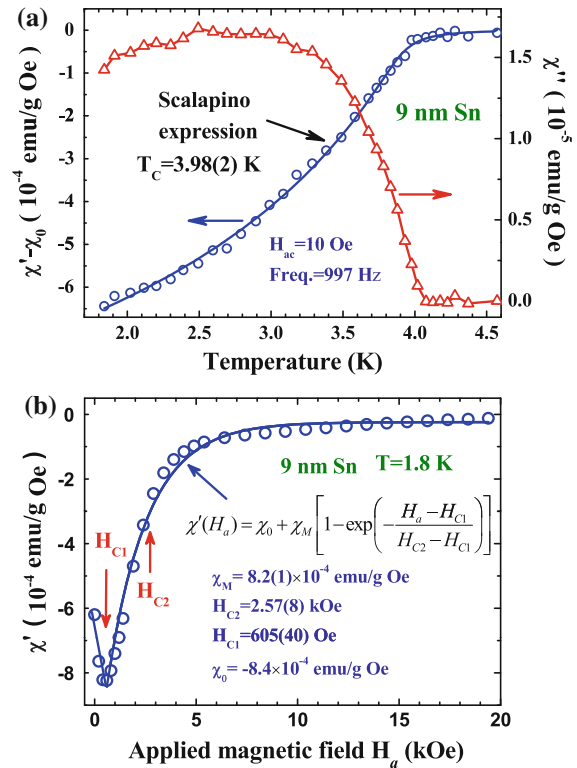


**Fig. 5** **a** Temperature dependencies of the in-phase  $\chi'$  and out-of-phase  $\chi''$  components of the ac magnetic susceptibility, measured using a probing field with a root-mean-square strength of 10 Oe and a frequency of 997 Hz. The *solid curve* on  $\chi'(T)$  indicates the fits of the data to Scalapino's expression for superconducting screening, giving a  $T_C = 3.98$  K. **b**  $\chi'(H_a)$  curve taken at 1.8 K, revealing a type-II like screening curve. The *solid curve* at above  $H_{C1}$  indicates the fits of the data to the expression listed in plot, giving an  $H_{C2} = 2.57$  kOe that indicates the  $H_a$  at which point diamagnetic screening reduces to 37 % of its maximum value

of  $\chi'$  by  $H_a$  can be described by an exponential profile (solid curve), as listed in the plot, to give  $H_{C2} = 2.57(8)$  kOe, which indicates the  $H_a$  at which point the superconducting screening has been reduced to 37 % of its maximum value. A 9 nm particle is far too small to accommodate even a single flux vortex. The gradual reductions of diamagnetic screening by  $H_a$  above  $H_{C1}$  cannot then arise from the appearance of flux vortices in the nanoparticles, but instead are due to the increase in penetration depth  $\lambda_L$  that in turn reduces the superconducting pair concentration, hence the shielding capability, of nanoparticles.

The existence of intrinsic magnetic moments in 9 nm Sn is confirmed by the neutron diffraction measurements. These measurements were conducted



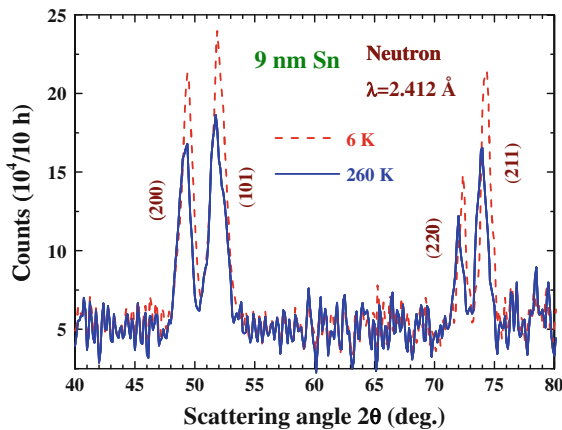


**Fig. 6** Direct comparisons of the neutron diffraction patterns of the 9 nm Sn particle assembly, taken at 260 (*bottom*) and 6 (*top*) K. Noticeable increases in the intensities are visible upon cooling

at the Bragg Institute, ANSTO, using the high intensity powder diffractometer Wombat, employing Ge(113) monochromator crystals to select an incident wavelength of  $\lambda = 2.412 \text{ \AA}$  and a cylindrical vanadium-can to hold the nanoparticles ( $\sim 0.7 \text{ g}$ ). Figure 6 displays the neutron diffraction patterns of the 9 nm particle assembly taken at 260 and 6 K for a direct comparison. The Bragg intensities of the 6 K pattern are noticeably more intense. It is interesting to note that the relative intensities of the peaks taken at 6 K are quite different from those taken at 260 K. The intensities of the {200}, {101}, {220}, and {211} reflections increase by 22, 27, 32, and 33 %, respectively, upon cooling from 260 to 6 K. These intensity increases are significantly higher than the 16 % increase expected from the reduction of Debye–Waller factor (DeWames et al. 1963), signaling the development of magnetic correlations upon cooling.

The diffraction patterns were analyzed using the GSAS program (Larson and von Dreele 1990), following the Rietveld profile refining method. The observed (crosses) and fitted (solid lines) patterns at 6 K, assuming a tetragonal  $\beta$ -Sn for the crystalline structure, are shown in Fig. 7a. There is a considerable amount of the (101) intensity that cannot be accounted for (marked by the arrow at the bottom), when assuming the Bragg intensities are solely generated by the crystalline structure. The calculated intensity of the (101) reflection is 9 % weaker than the (200) intensity, whereas the observed one is 16 % stronger. Magnetic contributions that provide a stronger intensity for

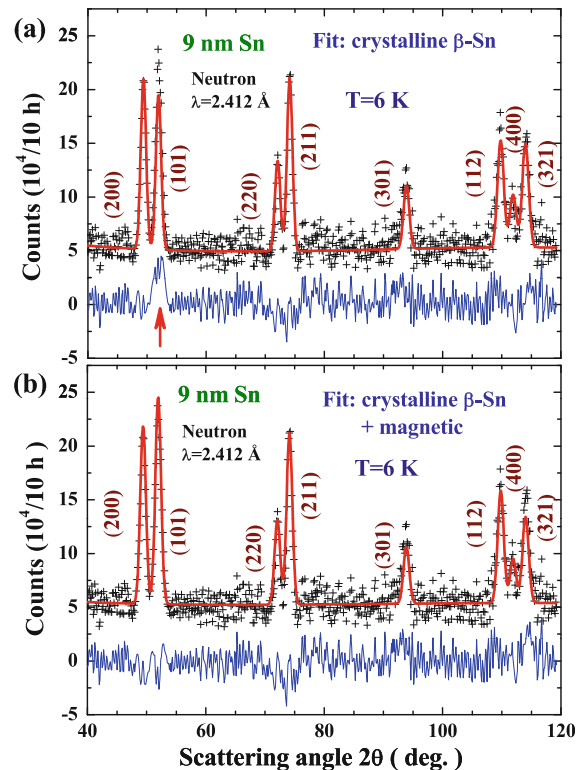


**Fig. 7** Observed (*crosses*) and profile refined (*solid lines*) neutron powder-diffraction patterns taken at 6 K, assuming **a** a tetragonal  $\beta$ -Sn crystalline structure and **b** a tetragonal  $\beta$ -Sn crystalline structure plus a ferromagnetic component for the Sn ions. The differences between the calculated and observed patterns are plotted at the *bottom*

the (101) reflection than for the (200) reflection is indeed needed to fully account the observations. Figure 7b shows the refined result (solid lines) when assuming an additional ferromagnetic component for the Sn ions. The observed intensities can then be better accounted for, when assuming a  $\beta$ -Sn crystalline structure together with a ferromagnetic moment of  $\langle \mu_z \rangle = 0.38 \mu_B$  that lies in the crystallographic  $a$ - $c$  plan but points  $10^\circ$  away from the tetragonal  $a$ -axis.

Figure 8 displays the difference pattern between the diffraction patterns taken at 1.65 and 6 K, revealing significant increases in the reflection intensities upon cooling through superconducting transition. These magnetic intensities appear on top of the nuclear ones, showing a ferromagnetic arrangement for the 9 nm Sn moments. The widths of the magnetic peaks are the same as those of the nuclear ones, indicating that the magnetic moments are distributed

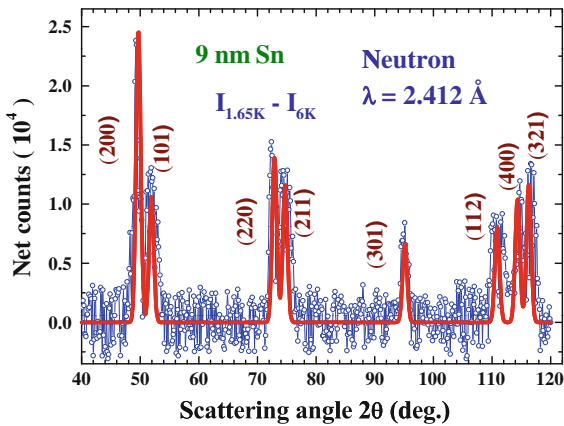


**Fig. 8** Difference pattern between the neutron diffraction patterns taken at 1.65 and 6 K, revealing the intensities in the superconducting state is significantly increased. The *solid curves* indicate the calculated pattern based on the magnetic structure discussed in text

throughout the whole nanoparticle, rather than being located solely on the surface. The difference pattern shown in Fig. 8 can be described (solid curve) reasonably well by assuming the development of a ferromagnetic moment of  $\langle \mu_z \rangle = 0.05 \mu_B$  that lies in the crystallographic *a-c* plan but points  $30^\circ$  away from the tetragonal *a*-axis. The temperature dependence of the (220) reflection is shown in Fig. 9, where the intensities have been modified by Debye–Waller factor to remove the effects from thermal atomic vibrations. The Debye–Waller factors used in intensity reduction at various temperatures were extracted from a previous report for bulk Sn (DeWames et al. 1963). No modification on the intensity data was made for temperatures below 10 K. The Debye–Waller modification factors employed for the 50, 100, 150, 200, and 260 K intensities were 0.958, 0.936, 0.913, 0.888, and 0.858, respectively.

There is a huge change in the thermal variation rate of the intensity at 4 K. In the normal state the (220) intensity increases by  $\sim 13\%$  upon cooling from 260 to 6 K. There is an additional  $5\%$  increase in the (220) intensity upon further cooling through superconducting transition, as can be seen in the inset to Fig. 9. The thermal reduction rates of the magnetic intensities in the normal state and in the superconducting state differ by a factor of more than 22, showing that they are associated with different origins. It is known that the magnetic intensity is proportional to the square of the magnetization. The temperature dependence of the

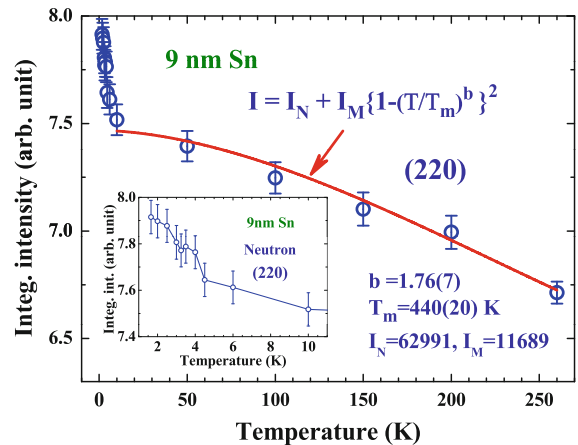


**Fig. 9** Temperature dependence of the (220) reflection, revealing a significant change in the thermal reduction of the intensity at 4 K. The *solid curve* indicates the fits of the data to Bloch’s law, giving a critical exponent of  $b = 1.76$ . The *inset* displays the low temperature portion of the curve using an expanded scale, showing further increases in the intensity on entering the superconducting state

(220) intensity above 6 K can be described (solid curve) by the square of Bloch’s expression, as listed in the plot, to give an exponent of  $b = 1.76(7)$ , which agrees very well with what is obtained from the  $M_S(T)$  curve shown in Fig. 3b.

The development of an additional magnetic moment in the superconducting state is also evident in the  $M(H_a)$  curves taken below  $T_C$ . They depart noticeably from the Langevin profile, as shown in the inset to Fig. 10. The magnetic component that is associated with the development of superconductivity can be clearly revealed in the difference magnetizations between the  $M(H_a)$  curves taken at 1.8 and 5 K, as shown in Fig. 10. The field-increasing (filled circles) and field-decreasing (open triangles) curves match above 6 kOe, showing that the effects link to superconductivity persists up to 6 kOe. The line profile of the field-increasing curve resembles that of  $\chi'(T)$  taken at 1.8 K (Fig. 5b), where an up-turn at 0.6 kOe and an anomaly at 2.5 kOe are clearly seen. The field-decreasing curve reflects the magnetization developed upon entering the superconducting state by the reduction of applied magnetic field. There are two main contributions: one from the further development of the magnetic component already exists in the normal state, and the other from that associated with the development of superconductivity. Positive values of  $\sim 0.015$  emu/g are obtained for  $M_{1.8K} - M_{5K}$  at high

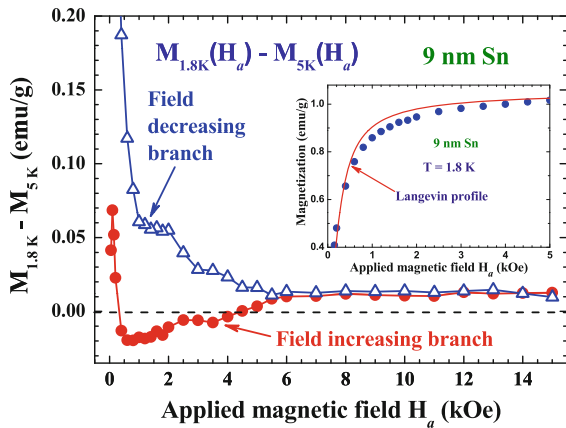


**Fig. 10** Difference magnetizations between the  $M(H_a)$  curves taken at 1.8 and 5 K. The field-increasing (filled circles) and field-decreasing (open triangles) curves match above 5 KOe. Two anomalies are clearly revealed in both the field-increasing and field-decreasing curves. The inset shows a portion of the  $M(H_a)$  curves taken at 1.8 K. It departs noticeably from the Langevin profile (solid line)

fields (Fig. 10), showing that the saturation magnetization increases  $\sim 0.015$  emu/g upon cooling from 5 to 1.8 K. The additional magnetizations appeared at low fields mark the magnetic moment developed in the superconducting state. There are two anomalies at 1 and 2.5 KOe in the field-decreasing curve, showing that the generation of this magnetic component is sensitive to  $H_a$ . Furthermore, the anomalies in the field-increasing curve appear at slightly weaker  $H_a$  than those in the field-decreasing curve, reflecting that the energy barrier at the particle surface for the entry of magnetic flux lines is lower than that for exit. We remark that a 9 nm Sn particle is far too small to accommodate even a single flux vortex. A BCS type-II scenario of accommodate magnetic flux inside the nanoparticle is not possible.

### Concluding remarks

The origins behind the development of magnetic moments in nanoparticles are not yet completely understood. They can nevertheless be associated with the reduction in the coordination number that modifies the band structure, with the lowering of structural symmetry that lifts degeneracy, or with the charges being transferred between the core and surface regions that result in an electronic charge redistribution (Alonso 2000; Isabelle et al. 1994; Khanna and

Linderoth 1991). 26 % of the Sn atoms in a 9 nm particle located on the surface shell that have a reduced coordination number. They can certainly play an important role in affecting the overall behavior of the nanoparticles. The surface atoms are more closely packed than the core ones due to the appearance of surface stress that deforms the surface of the nanoparticle making it curved. Electron transfer from the surface region to the core region can be anticipated in leveling the Fermi energy of the two regions. As a result, the number of uncompensated spins in the nanoparticle increases, which in turn gives rise to a distribution of localized magnetic moments over the nanoparticles and a net particle moment. Another possible source of ferromagnetism is the appearance of orbital moments induced in atomic-like localized states by intra-orbital ferromagnetic spin correlations. This orbital magnetism can appear under the combination of spin-orbit coupling and contact potential at the nanoparticle boundaries. In such circumstances, the electrostatic interactions between the electrons trapped in the same orbit can initiate a spin arrangement, which subsequently induces an orbital moment alignment through spin-orbit interactions. This type of orbital ferromagnetism has been used (Hernando et al. 2006) to understand the magnetic moment observed in thiol-capped Au films and nanoparticles. It, however, is still surprising that a 9 nm Sn particle can develop such a large magnetic moment, reaching 2 % that of bulk Ni.

It is clear that the superconductivity that operates in the present Sn nanoparticles is different in nature from that which operates in bulk Sn. The quantum confinement is not yet significant in the present nanoparticles. There are, nevertheless, at least three factors that can affect the development of superconductivity in Sn nanoparticles: First, the small size effect can trigger electronic charge redistribution (Fig. 2). Second, charge transfer between the surface and core regions can result in a redistribution of conduction electrons that alters the available conduction electron density for Cooper pairing. Third, the internal magnetic field generated by the magnetic moments in the particle can also suppress the formations of Cooper pairs. Unfortunately, it is not feasible to draw a conclusion on the importance of each factor in the present study. The present study shows that the ferromagnetism can develop in 9 nm Sn particles,  $\beta$ -Sn supports superconductivity better than  $\alpha$ -Sn does, and more



importantly a magnetic moment can be associated with superconductivity.

**Acknowledgments** We thank ANSTO for providing Wombat beam time that makes neutron diffraction measurements possible. This study was supported by the National Science Council of Taiwan under Grant No. NSC 101-2112-M-008-016-MY3.

## References

- Alonso JA (2000) Electronic and atomic structure, and magnetism of transition-metal clusters. *Chem Rev* 100:637. doi:[10.1021/cr980391o](https://doi.org/10.1021/cr980391o)
- Bezryadin A, Lau CN, Tinkham M (2000) Quantum suppression of superconductivity in ultrathin nanowires. *Nature* 404:971–974. doi:[10.1038/35010060](https://doi.org/10.1038/35010060)
- Bose S, Raychaudhuri P, Banerjee R, Vasa P, Ayyub P (2005) Mechanism of the size dependence of the superconducting transition of nanostructured Nb. *Phys Rev Lett* 95:147003. doi:[10.1103/PhysRevLett.95.147003](https://doi.org/10.1103/PhysRevLett.95.147003)
- Bose S, Garcia-García AM, Ugeda MM, Urbina JD, Michaelis CH, Brihuega I, Kern K (2010) Observation of shell effects in superconducting nanoparticles of Sn. *Nat Mater* 9:550–554. doi:[10.1038/nmat2768](https://doi.org/10.1038/nmat2768)
- Crespo P, Litrán R, Rojas TC, Multigner M, de la Fuente JM, Sánchez-López JC, García MA, Hernando A, Penadés S, Fernández A (2004) Permanent magnetism, magnetic anisotropy, and hysteresis of thiol-capped gold nanoparticles. *Phys Rev Lett* 93:087204. doi:[10.1103/PhysRevLett.93.087204](https://doi.org/10.1103/PhysRevLett.93.087204)
- DeWames RE, Wolfram T, Lehman GW (1963) Temperature dependence and anisotropy in the Debye–Waller factor for white tin. *Phys Rev* 131:529. doi:[10.1103/PhysRev.131.529](https://doi.org/10.1103/PhysRev.131.529)
- Duffy JA, Hayden SM, Maeno Y, Mao Z, Kulda J, McIntyre GJ (2000) Polarized-neutron scattering study of the Cooper-pair moment in Sr<sub>2</sub>RuO<sub>4</sub>. *Phys Rev Lett* 85:5412. doi:[10.1103/PhysRevLett.85.5412](https://doi.org/10.1103/PhysRevLett.85.5412)
- Guo Y, Zhang YF, Bao X-Y, Han T-Z, Tang Z, Zhang L-X, Zhu W-G, Wang EG, Niu Q, Qiu ZQ, Jia JF, Zhao Z-X, Xue Q-K (2004) Superconductivity modulated by quantum size effects. *Science* 306:1915–1917. doi:[10.1126/science.1105130](https://doi.org/10.1126/science.1105130)
- Halperin WP (1986) Quantum size effects in metal particles. *Rev Mod Phys* 58:533. doi:[10.1103/RevModPhys.58.533](https://doi.org/10.1103/RevModPhys.58.533)
- Hendriksen PV, Linderroth S, Lindgård P-A (1992) Finite-size effects in the magnetic properties of ferromagnetic clusters. *J Magn Magn Mater* 104–107:1577. doi:[10.1016/0304-8853\(92\)91461-2](https://doi.org/10.1016/0304-8853(92)91461-2)
- Hernando A, Crespo P, García MA (2006) Origin of orbital ferromagnetism and giant magnetic anisotropy at the nanoscale. *Phys Rev Lett* 96:057206. doi:[10.1103/PhysRevLett.96.057206](https://doi.org/10.1103/PhysRevLett.96.057206)
- Hori H, Yamamoto Y, Iwamoto T, Miura T, Teranishi T, Miyake M (2004) Diameter dependence of ferromagnetic spin moment in Au nanocrystals. *Phys Rev B* 69:174411. doi:[10.1103/PhysRevB.69.174411](https://doi.org/10.1103/PhysRevB.69.174411)
- Isabelle ML, Châtelain A, de Heer WA (1994) Magnetism from the atom to the bulk in iron, cobalt, and nickel clusters. *Science* 265:1682. doi:[10.1126/science.265.5179.1682](https://doi.org/10.1126/science.265.5179.1682)
- Karna SK, Li C-Y, Wu C-M, Hsu C-K, Wang C-W, Li W-H (2011) Observations of large magnetic moments in icosahedral Pb nanoparticles. *J Phys Chem C* 115:8906. doi:[10.1021/jp1118212](https://doi.org/10.1021/jp1118212)
- Khanna SN, Linderroth S (1991) Magnetic behavior of clusters of ferromagnetic transition metals. *Phys Rev Lett* 67:742. doi:[10.1103/PhysRevLett.67.742](https://doi.org/10.1103/PhysRevLett.67.742)
- Kittel C (1996) Introduction to solid state physics, 7th edn. Wiley, New York, pp 446–448
- Larson AC, Von Dreele RB (1990) General structure analysis system. Los Alamos National Laboratory Report LAUR-86-748
- LeClair P, Moodera JS, Philip J, Heiman D (2005) Coexistence of ferromagnetism and superconductivity in Ni/Bi bilayers. *Phys Rev Lett* 94:037006. doi:[10.1103/PhysRevLett.94.037006](https://doi.org/10.1103/PhysRevLett.94.037006)
- Li W-H, Yang CC, Tsao FC, Lee KC (2003) Quantum size effects on the superconducting parameters of zero-dimensional Pb nanoparticles. *Phys Rev B* 68:184507. doi:[10.1103/PhysRevB.68.184507](https://doi.org/10.1103/PhysRevB.68.184507)
- Li W-H, Yang CC, Tsao FC, Wu SY, Huang PJ, Chung MK, Yao YD (2005) Enhancement of superconductivity by the small size effect in In nanoparticles. *Phys Rev B* 72:214516. doi:[10.1103/PhysRevB.72.214516](https://doi.org/10.1103/PhysRevB.72.214516)
- Li W-H, Wang C-W, Li C-Y, Hsu CK, Yang CC, Wu C-M (2008) Coexistence of ferromagnetism and superconductivity in Sn nanoparticles. *Phys Rev B* 77:094508. doi:[10.1103/PhysRevB.77.094508](https://doi.org/10.1103/PhysRevB.77.094508)
- Liu S-B, Chen C-T, Wu C-M, Wang C-W, Wang C-J, Karna SK, Li W-H (2011) Suppression of superconductivity by interparticle interactions in Al nanoparticle assembly. *J Appl Phys* 109:07E153. doi:[10.1063/1.3564936](https://doi.org/10.1063/1.3564936)
- Mühschlegel B, Scalapino DJ, Dento R (1972) Thermodynamic properties of small superconducting particles. *Phys Rev B* 6:1767. doi:[10.1103/PhysRevB.6.1767](https://doi.org/10.1103/PhysRevB.6.1767)
- Reich S, Leitus G, Popovitz-Biro R, Schechter M (2003) Magnetization of small lead particles. *Phys Rev Lett* 91:147001. doi:[10.1103/PhysRevLett.91.147001](https://doi.org/10.1103/PhysRevLett.91.147001)
- Wu C-M, Li C-Y, Kuo Y-T, Wang C-W, Wu S-Y, Li W-H (2010) Quantum spins in Mackay icosahedral gold nanoparticles. *J Nanopart Res* 12:177–185. doi:[10.1007/s11051-009-9592-3](https://doi.org/10.1007/s11051-009-9592-3)
- Yamamoto Y, Miura T, Suzuki M, Kawamura N, Miyagawa H, Nakamura T, Kobayashi K, Teranishi T, Hori H (2004) Direct observation of ferromagnetic spin polarization in gold nanoparticles. *Phys Rev Lett* 93:116801. doi:[10.1103/PhysRevLett.93.116801](https://doi.org/10.1103/PhysRevLett.93.116801)